minerals

MDPI

Article

Jianite: Massive Dunite Solely Made of Virtually Pure Forsterite from Ji'an County, Jilin Province, Northeast China

Yuwei Wang [1], Mingyue He [1,*], Wei Yan [2,3], Mei Yang [1] and Xi Liu [2,3,*]

[1] School of Gemmology, China University of Geosciences (Beijing), Beijing 100083, China; 2009170014@cugb.edu.cn (Y.W.); yangmei@cugb.edu.cn (M.Y.)
[2] School of Earth and Space Sciences, Peking University, Beijing 100871, China; wei.yan@pku.edu.cn
[3] Key Laboratory of Orogenic Belts and Crustal Evolution, Ministry of Education of China, Beijing 100871, China
* Correspondence: hemy@cugb.edu.cn (M.H.); xi.liu@pku.edu.cn (X.L.); Tel.: +86-10-6275-3585 (X.L.); Fax: +86-10-6275-2996 (X.L.)

Received: 1 February 2020; Accepted: 26 February 2020; Published: 29 February 2020

Abstract: A rare massive yellowish-green serpentinized dunite, covering a minimum area up to ~50 m^2, has been found in Ji'an County, Jilin Province, Northeast China. It contains primary olivine and secondary serpentine (antigorite) and brucite. Other primary minerals like orthopyroxene, clinopyroxene, and aluminum-rich phase (such as garnet, spinel, and plagioclase), frequently appearing in ultramafic rocks, have not been identified. The olivine is essentially pure forsterite, with an Mg# (100 × Mg/(Mg + Fe)) of ~99.6–99.7. Due to these distinct features, we especially name the protolith of this dunite as jianite (集安岩). The forsterite grains range up to ~2 mm, show clear equilibrium textures such as nearly straight grain boundaries and ~120° dihedral angles at their triple junctions, and display no intragranular or intergranular composition variations. They are extensively ruptured and hydrated (i.e., serpentinized), with the fractures (and the grain boundaries as well) filled by fine-grained antigorite (ideally $Mg_6(Si_4O_{10})(OH)_8$) and brucite (ideally $Mg(OH)_2$). These secondary phases are also extremely poor in Fe, indicating a good chemical equilibrium with the forsterite. The serpentinization reaction may have proceeded as forsterite + fluid = antigorite + brucite at temperatures of ~425(25) °C and at relatively low but undetermined pressures. The fluid was likely a B-rich, but Si-poor dilute aqueous fluid, as implied by the trace element characteristics and water-related infrared features of the forsterites in equilibrium. The petrogenesis of the jianite is presently unclear.

Keywords: antigorite; brucite; massive dunite; forsteritic olivine; hydration; jianite

1. Introduction

The ultramafic peridotitic upper mantle generally consists of olivine (Ol; $(Mg,Fe)_2SiO_4$), orthopyroxene, clinopyroxene, and an aluminous phase (plagioclase, spinel or garnet, depending on pressure). As it partially melts to generate basaltic magmas, it gradually turns into harzburgite and dunite, with the former containing olivine, orthopyroxene, and the aluminous phase (small amount), and the latter containing olivine and the aluminous phase (trace amount). Subject to the interior thermal state of the Earth, this partial melting process seldom goes beyond the elimination of orthopyroxene, so that a residual dunite is rarely generated [1,2]. Indeed, mantle xenoliths brought up by kimberlites and alkaline basalts are usually lherzolite and harzburgite [3–5] and only sparsely dunite [6,7].

As the partial melting process progresses, the constituent phases of the peridotite alter their compositions and become more refractory. High-*P* experiments and field observations suggest that

the Mg# (100 × Mg/(Mg + Fe)) of the residual olivine increases from a typical mantle value of ~89 to ~95 [2,3,8,9], and the Cr# (100 × Cr/(Cr + Al)) of the residual spinel sharply increases from ~20 to over 80 [2,10,11]. Further, the magmas derived from this partial melting process are incapable of crystallizing at shallow depths more refractory olivine (with Mg# higher than that of the corresponding residual olivine in the source regions) due to the Fe-Mg partitioning equilibrium [12,13]. Consequently, natural olivine with Mg# > 96 is not typical for any igneous rocks in general [14]. Natural olivine crystals with nearly pure forsteritic composition (with Mg# > 96) were sometimes found as phenocrysts in some basalts and kimberlites [15,16], as inclusions in chromites from some podiform chromitite [17], and as one of the metamorphic minerals in the contact zone between an igneous rock and a carbonate rock [18–20]. Their genesis has been attributed to some special processes such as subsurface oxidation, subsolidus re-equilibration, and interaction with carbonates [14]. Additionally, narrow pseudomorphic olivine rims with Mg# > 96 were occasionally found surrounding primary olivine grains (Mg# = ~89–92) in some serpentinites, with their genesis ascribed to the serpentinization or deserpentinization reaction [21–23].

Here, we report a massive serpentinized dunite (occupying an area of at least up to ~50 m^2) from Ji'an County, Jilin Province, Northeast China. The protolith of this rock contains virtually pure forsterite (i.e., Mg# = ~100), which coexist with no other primary mantle phase. This type of lithology is extremely rare and has not been well characterized so far.

2. Sampling Location and Analytical Methods

The sampling area lies to the east of the Songliao depression and consists of four major tectonic terranes, the Ji-Hei orogenic belt, the Longgang block, the Liao-Ji Proterozoic rift zone, and the Langlin block (Figure 1).

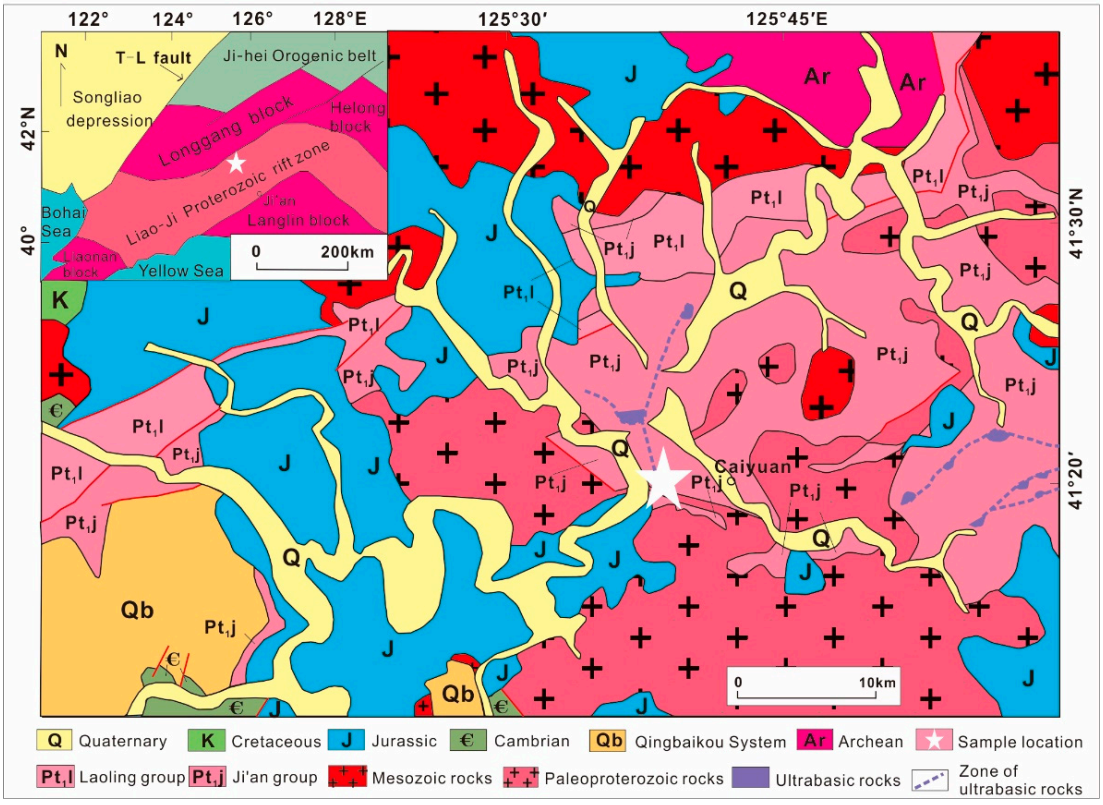

Figure 1. Geological map of the sample-collecting area (after Qin et al. [24]; Zhou et al. [25]). The exact sample-collecting location is indicated by the white star (latitude N41°20′18″, longitude E125°39′). The insert shows the major tectonic terranes in a much larger area. T-L fault refers to the Tancheng–Lujiang fault.

The rock documented here exposes in the Mayihe formation of the Ji'an group, which locates in the Liao-Ji Proterozoic rift zone. The Mayihe formation, a boron-bearing sequence with a deposition age of ~2126–1940 Ma [26], contains various altered felsic and granitic rocks, dolomitic marble, serpentinized olivine marble, and boron- and iron-bearing serpentinite, and amphibolite [24,27]. It has been proposed that some metavolcanic rocks of the Ji'an group formed at ~2189–2156 Ma and experienced an amphibolite facies metamorphic event at ~1881–1870 Ma [24]. Existing petrochemical and geochemical analyses of the altered volcanic rocks show the characteristics of the calc-alkali volcanic rocks of island arc, indicating the possible involvement of an ancient subduction process [28]. Recently, some ultra-basic rock blocks were found in the metamorphic sedimentary rocks of the Ji'an group [25].

The discovered outcrop of the serpentinized dunite locates near Jiayi Village, Caiyuan Town, Ji'an County, Jilin Province. The exposed body, with a yellowish weathered surface, is ~10–15 m long, ~4–5 m wide, and ~3–4 m high (Figure 2). The rock contains olivine, serpentine (Serp), and brucite (Brc), and shows varying degrees of serpentinization. The relatively dark neighboring rock (Figure 2b) is of similar lithology but presumably has a different bulk composition (to be reported elsewhere). A large number of specimens were collected from the serpentinized dunite. Here, we have arbitrarily selected and subsequently processed four samples (JAY01, JAY02, JAY03, and JAY04) to investigate the basic petrological and mineralogical features.

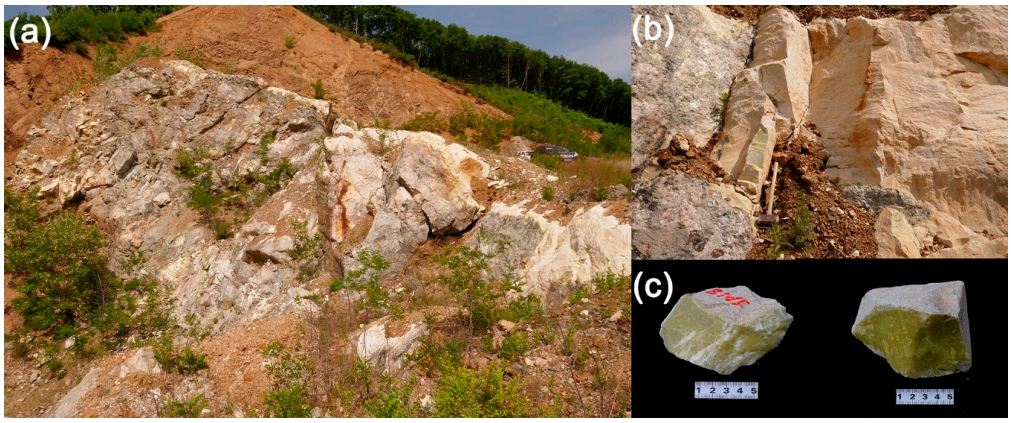

Figure 2. Photographs of jianite: (**a**) Full field view of the outcrop, which is ~10–15 m long and ~4–5 m wide; (**b**) A close-up view of the outcrop; (**c**) Representative photo of two specimens.

The textures of the samples were examined by using a SUPRA 55 scanning electron microscope (SEM) hosted at the China University of Geosciences (Beijing). The accelerating voltage was 20 kV. The constituent phases were identified by using a Renishaw inVia Reflex microscope equipped with a 532 nm laser in a back-scattering geometry [29]. Other experimental conditions included a laser emission power of ~50 mW, a 50× objective, and a data-collecting range of 100–4000 cm^{-1}. Every Raman spectrum was obtained by averaging 10 successive scans with 1 cm^{-1} resolution (10 s for each scan). The major element concentrations of the minerals were obtained by using a JXA-8230 electron microprobe (EMP) analyzer hosted by the MOE Key Laboratory of Orogenic Belts and Crustal Evolution, Peking University. The analytical conditions were an acceleration voltage of 15 kV, a beam current of 10 nA, a beam diameter of 1–2 μm, and a counting time of 10–15 s [30]. The calibration was based on optimization to some standards provided by the SPI Corporation (USA), with sanidine for K, diopside for Ca and Mg, rutile for Ti, jadeite for Na, Al, and Si, chromium oxide for Cr, rhodonite for Mn, hematite for Fe, and nickel silicide for Ni [29]. The data reduction was executed with the PRZ correction procedure.

The trace elements ^{7}Li, ^{11}B, ^{23}Na, ^{24}Mg, ^{27}Al, ^{31}P, ^{43}Ca, ^{44}Ca, ^{45}Sc, ^{47}Ti, ^{49}Ti, ^{51}V, ^{53}Cr, ^{55}Mn, ^{59}Co, ^{60}Ni, ^{63}Cu, ^{66}Zn, ^{69}Ga, ^{88}Sr, ^{89}Y, ^{90}Zr, ^{93}Nb, and ^{140}Ce of the olivine were analyzed by using an Agilent 7500 Ce laser ablation inductively coupled plasma mass spectrometry (LA-ICP-MS) hosted by the MOE

Key Laboratory of Orogenic Belts and Crustal Evolution, Peking University. The LA-ICP-MS system was coupled to a COMPexPro 102 laser-ablation system with a 193 nm ArF-excimer laser [31]. Helium was served as the carrier gas to enhance the transport efficiency of the ablated material. Each analysis comprised ~20 s background acquisition (gas blank) followed by 60 s data acquisition [32]. The beam was set to a diameter of ~60 μm with a repetition rate of 5 Hz and laser energy of 100 mJ. The NIST glass 610 was used as an external standard, the NIST glasses 612 and 614 were used as monitoring standards [33], and the ^{24}Mg content obtained by the EMP analyses was used as an internal standard. Homogeneous sections of the signals were selected to derive the results so that the influences of any potential inclusions and fractionations encountered by the laser beam could be removed. The final data reduction was carried out using the Glitter software package [34].

The water content of the olivine was examined by using a Nicolet iN10 MX IR Microscope, which was equipped with a high-energy Ever-Glo^{TM} infrared source, a standard KBr beam splitter, and a liquid-nitrogen-cooled MCT detector at the High-Pressure Laboratory of Peking University [35,36]. Transmission IR spectra were collected on olivine crystals or fragments from a free-standing, doubly polished thin section. To make the thin section, the general preparing procedure outlined in Liu et al. [37] was followed. Firstly, a slice of rock cut off from the specimen JAY04 by using a low-speed diamond saw was placed on a glass slide with some crystal-bond, and subsequently reduced to a thickness of ~160 μm by using a series of silicon carbide abrasive papers. The thickness of the final rock thin section was determined by utilizing a digital micrometer, and the accuracy of the measurement was ~2 μm. Secondly, the rock thin section was thoroughly washed in acetone for 24 h to dissolve the crystal-bond, cleaned in ethanol for several times, and dried at ~110 °C for several hours. Thirdly, 11 clean olivine crystal plates (or fragments from different olivine crystals) with no discernible cracks or inclusions were manually picked up under an optical microscope, transferred and placed on a BaF_2 sample holder, and analyzed by the FTIR. The spectra from 7800 to 675 cm^{-1} were recorded with an aperture of 50 × 50 μm^2, 512 scans, and a resolution of 4 cm^{-1}. The data were processed by using the OMNIC8 software and PeakFit V4.12 software.

3. Results

3.1. Petrography

The rock contains roughly 60% olivine, 30% serpentine, and 10% brucite, with olivine clearly as a primary phase and serpentine and brucite as secondary phases (Figure 3). The olivine grains, often up to ~2 mm in diameter, are extensively fractured, with the fractures (and the grain boundaries as well) filled by fine-grained serpentine aggregates and brucite aggregates. This spatial arrangement obviously indicates the following hydration reaction (i.e., serpentinization reaction),

$$\text{olivine} + \text{fluid} = \text{serpentine} + \text{brucite} \quad (1)$$

In general, the hydration zones along the grain boundaries of the olivines, with coarser serpentine and brucite grains, are wider than those in the fractures within the olivine grains, indicating a hierarchic fluid-transport system operating in the hydration process (Figure 4). Both along the grain boundaries and in the fractures of the olivine grains, the serpentine aggregates, appearing as layers, often locate themselves next to the olivines and sandwich the layers of the brucite aggregates. This phenomenon might imply that, if both the Mg cations and the Si cations contained by the serpentines and brucites were from the olivines, the Mg cations would have diffused much faster than the Si cations in the fluid, leading to the crystallization of the serpentines near the olivines and the crystallization of the brucites slightly farther away. In addition, we expect that the serpentinization reaction should have hardly approached its completion due to the gradual isolation of the olivine grains from the fluid by the serpentine aggregates and brucite aggregates.

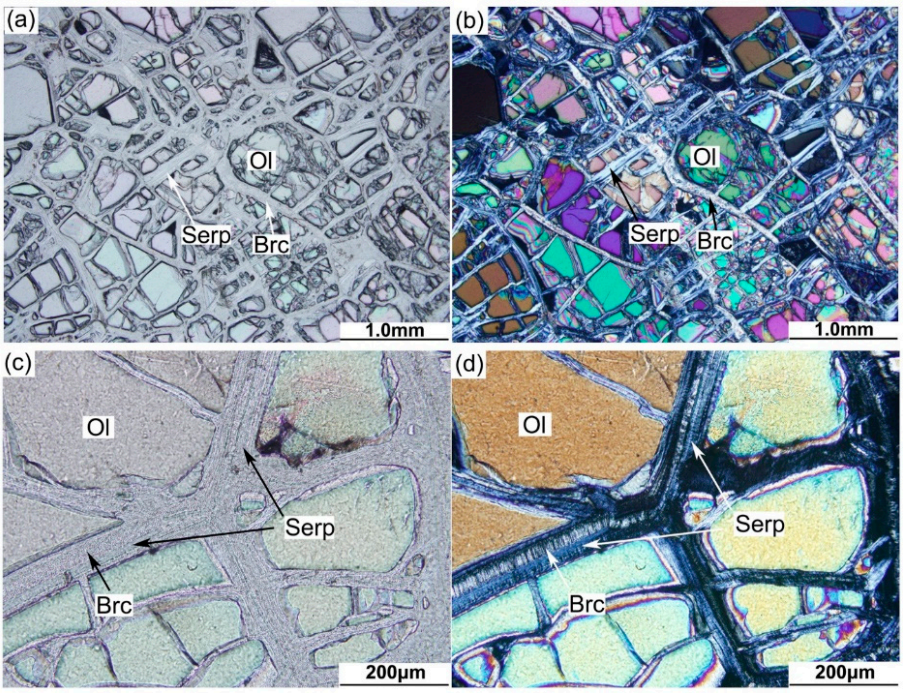

Figure 3. Photomicrographs of jianite (plane light on the left and crossed light on the right): (**a**,**b**) representing typical views (40×); (**c**,**d**) representing close-up views (200×). Ol, olivine; Serp, serpentine; Brc, brucite. Despite the strong disruption and extensive hydration, the initial crystallographic orientations of the olivine grains have been well preserved, as indicated by the almost identical extinction angles of the different fractions from the same olivine crystals. Note the ~120° dihedral angels at the triple junction shown in (**c**,**d**).

The observed phase assemblage, olivine + serpentine + brucite + fluid, in the rock generally indicates a *T* of ~425(25) °C and a wide *P* range of ~0–10 kbar for the hydration reaction [38,39]. At this high *T*, the cation diffusion rates are generally fast, and the compositions of the olivines and serpentines can be adequately adjusted, leading to no precipitation of magnetite and no formation of hydrogen [40,41]. Indeed, no magnetite has been detected so far.

The textures of the protolith of this rock seemingly have escaped the hydration process at least to some extent. The severely hydrated olivines usually contain numerous tiny inclusions (presumably serpentines) likely appearing along some special but undetermined crystallographic orientations (Figure 4a). In contrast, the less hydrated olivine grains are usually inclusion-free (Figure 4b). Whatever the extents of the hydration reaction are, the initial crystallographic orientations of the olivine grains have been well preserved, as indicated by the almost identical extinction angles of the different fragments from the same olivine crystals (Figure 3b,d). Further, the initial equilibrium texture of the olivine grains seems also well preserved, as implied by the nearly 120° dihedral angels at the triple junctions (Figure 3d).

Distinctly, orthopyroxene, clinopyroxene, garnet, spinel, plagioclase, and other minerals frequently encountered in the ultramafic rocks have not been found in the rock so far.

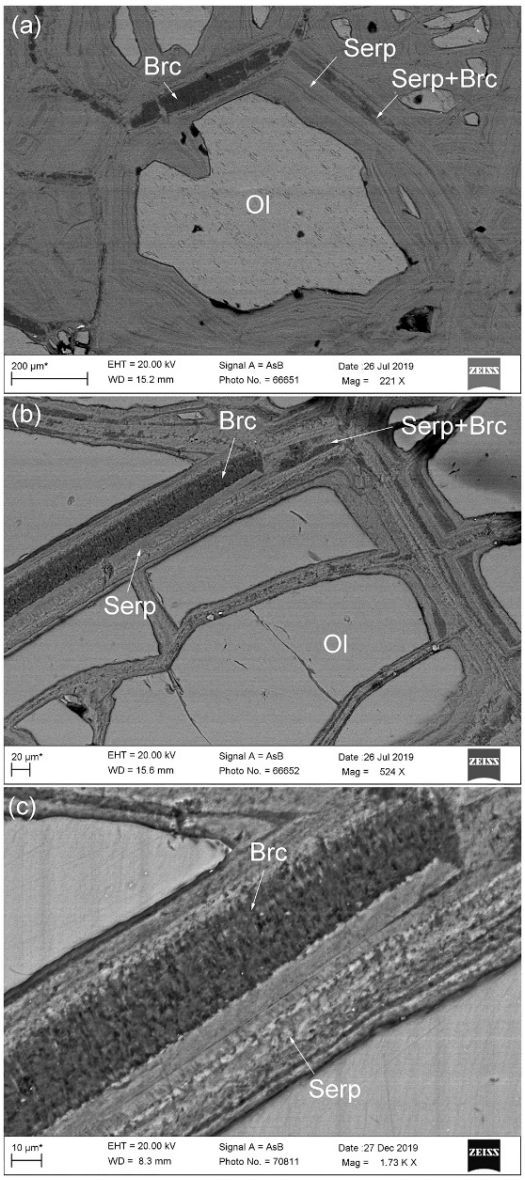

Figure 4. Representative electron back-scatter (BSE) images of jianite displaying various degrees of hydration and a hierarchic fluid-transporting system. (**a**) The olivine grain in the middle (surrounded by serpentine and brucite), in which needle-shaped fine mineral inclusions align along certain special crystallographic orientation, shows relatively weak serpentinization. In comparison, the olivine grain in the upper left part of the image (broken down into several relatively large olivine fragments) shows relatively strong serpentinization, that in the upper right part (broken down into many relatively small olivine fragments) shows strong serpentinization, and that either in the left part or in the right part (completely replaced by serpentine and brucite) shows complete serpentinization. (**b**) A hierarchic fluid-transporting system displayed by grain boundaries and cracks of different widths (from > 60 to < 10 µm) near a ruptured olivine grain, which is filled with serpentine aggregates and brucite aggregates. The examined area is generally the lower left part of the sample shown in Figure 3c,d. In most cracks, two layers of serpentine aggregates, thick or thin, generally occur next to the olivines and sandwich a layer of brucite aggregates. In some cases, the serpentine aggregates and brucite aggregates may form interbedded thin layers and display complicated textures. (**c**) A close-up view of the serpentine aggregates and brucite aggregates along the grain boundary in the upper left part of (**b**). Note that the olivine grain is almost inclusion-free, suggesting a weak serpentinization reaction. Ol, olivine; Serp, serpentine; Brc, brucite.

3.2. Phase Identification

The primary olivine has been identified as nearly pure forsterite (Fo) and the secondary serpentine as antigorite (Atg) by resorting to Raman spectroscopy. The identity of the secondary brucite has also been confirmed by our Raman data. No other phases have been suggested by the Raman spectra so far.

Representative Raman spectra for the primary olivines investigated here are shown in Figure 5, along with a reference Raman spectrum of the synthetic forsterite from Liu et al. [29]. The most prominent Raman peaks of olivine are those two occurring in the spectral regions of 815–825 and 838–857 cm^{-1}. As the Mg# of olivine rises, they should both shift from low wavenumbers toward high wavenumbers, and respectively reach the wavenumbers of ~825 and 857 cm^{-1} for the forsterite composition [42,43]. Our Raman spectra show these two peaks, respectively, at ~824 and 857 cm^{-1}, suggesting that these olivines should have compositions close to the forsterite, i.e., with extremely low Fe.

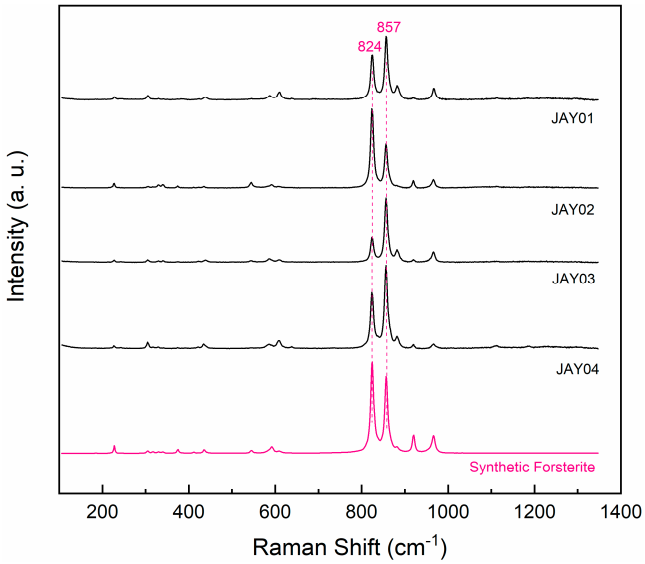

Figure 5. Typical Raman spectra of the olivines from jianite. Text next to the Raman spectrum is the label of the sample (JAY01, JAY02, JAY03, or JAY04). The Raman spectrum of the synthetic forsterite (Mg# = 100) is from Liu et al. [29]. The major Raman feature of the olivine is the two peaks occurring at ~815–825 cm^{-1} and ~838–857 cm^{-1}. To illustrate clearly, only one Raman spectrum is shown for each sample, although multiple Raman spectra have been collected.

Typical Raman spectra of the secondary serpentine phase are shown in Figure 6. They demonstrate a prominent peak at ~230 cm^{-1}, which is one of the characteristic Raman signals for antigorite [44–46]. In comparison, lizardite usually shows a Raman peak at a slightly higher wavenumber like ~233 cm^{-1} [47], ~234 cm^{-1} [48], or ~236 cm^{-1} [45], with a relatively low intensity [44]. The possibility of lizardite can thus be ruled out. Chrysotile may have a strong Raman peak at a similar wavenumber of ~231 cm^{-1} [47], which, however, mostly negatively correlates with the Al contents [45]. For Al-poor chrysotile, this Raman peak occurs at ~235 cm^{-1} [45]. Our serpentine contains no Al (with a chemical formula close to $Mg_6Si_4O_{10}(OH)_8$; to be shown later), and hence cannot be chrysotile. Briefly, our Raman data have identified the serpentine as antigorite. This conclusion is in agreement with all existing investigations. According to Evans [39,40] and Schwartz et al. [49], the stable serpentine polymorph at the *P-T* conditions of ~425(25) °C and ~0–10 kbar should be antigorite.

Typical Raman spectra of the secondary brucite phase are shown in Figure 7, along with a reference Raman spectrum for brucite and one Raman spectrum for antigorite. Although the Raman spectra have been somewhat contaminated by neighboring antigorites because of the small grain size of the brucites, the characteristic Raman peaks of brucite can be clearly observed at ~279 and 443 cm^{-1} [50,51], confirming the identity of the brucite.

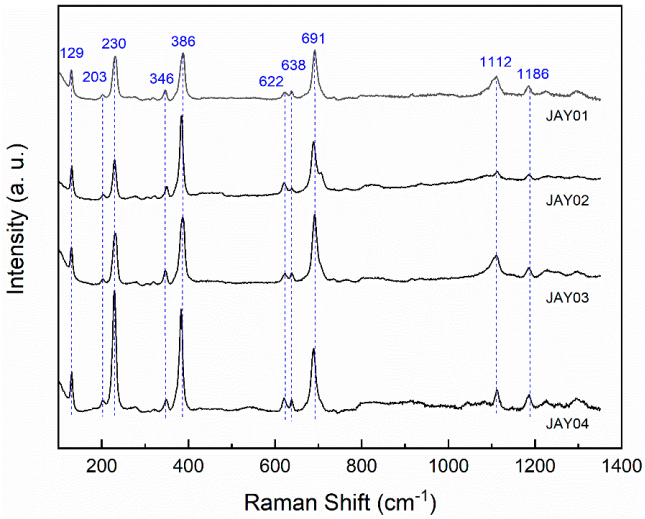

Figure 6. Typical Raman spectra of the large serpentines (antigorites) from jianite. Note that the Raman spectra from different samples (labeled with the text next to the spectrum) are almost identical. To illustrate clearly, only one Raman spectrum is shown for each sample, although multiple Raman spectra have been collected.

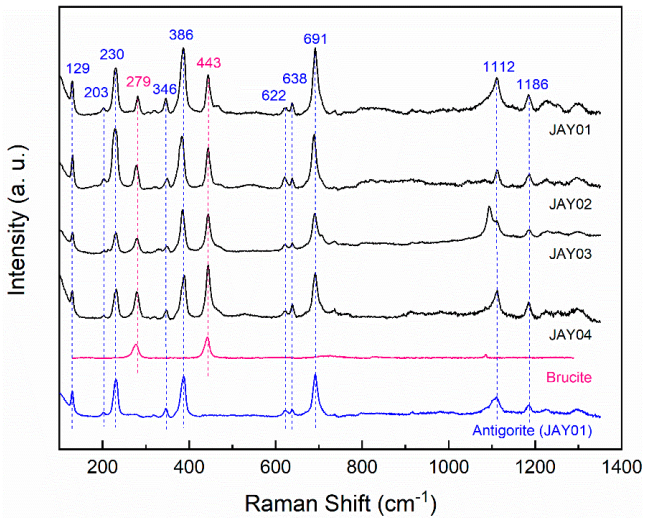

Figure 7. Typical Raman spectra of the brucite grains. Reference spectra for serpentine (blue) and brucite (pink) are respectively from Figure 6 (JAY01) or downloaded from the RRUFF Project website (http://rruff.info). Due to the small grain sizes of the brucite, its Raman spectra have been contaminated by nearby antigorites. To illustrate clearly, only one Raman spectrum is shown for each sample (labeled with the text next to the spectrum), although multiple Raman spectra have been collected.

Natural antigorite is relatively scarce [52] and usually contains significant amounts of Fe and Al [44,45]. As a result, no Raman data for any Fe- and Al-poor natural antigorite approximating the $Mg_6Si_4O_{10}(OH)_8$ composition has been reported. Reynard and Wunder [46] reported a Raman spectrum for a synthetic antigorite with the $Mg_6Si_4O_{10}(OH)_8$ composition, with many bands displaying small splitting, exhibiting shoulders, and being broad. Our antigorite has a composition close to the $Mg_6Si_4O_{10}(OH)_8$ formula, and its Raman spectrum should be very informative. Figure 8 shows the Raman spectra (for the intensity data see Supplementary Table S1).

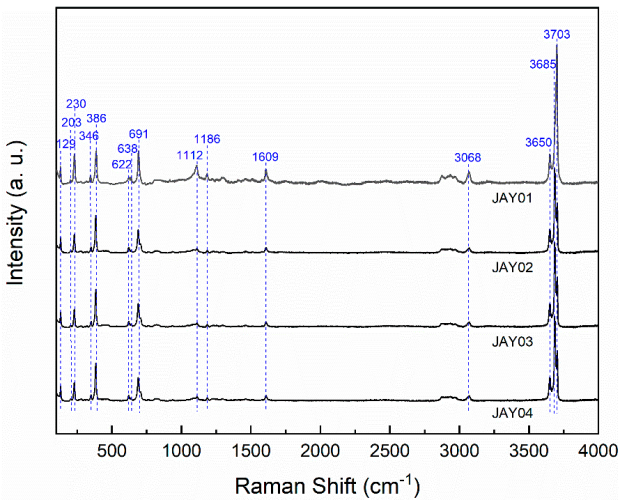

Figure 8. Raman spectra (in the range of 100–4000 cm^{-1}) of the nearly Fe-free and Al-free antigorites ($Mg_6Si_4O_{10}(OH)_8$) found in jianite. Note that the Raman spectra from different samples (labeled with the text next to the spectrum) are almost identical.

3.3. Chemistry of Minerals

The EMP analyses, performed on the rims, the mantles, and the cores of some randomly selected olivine grains (or fragments), are summarized in Table 1. The distinct compositional feature of the primary olivine is an unusually high Mg#, ranging from ~99.67(3) at the rims to ~99.64(1) at the cores so that these olivines are virtually homogeneous forsterites with extremely limited Mg-Fe variations (Figure 9). In addition, these forsterites are likely slightly short in Si (i.e., less than 1 Si per formula unit), especially for their rims, implying a low SiO_2 activity for the interacting fluid.

Table 1. Major element compositions (wt%) of olivines in the jianite.

	Rim(10) [a]	Mantle(10)	Core(5)
SiO_2	40.90(158)[b]	41.29(55)	41.32(47)
TiO_2	0.02(2)	0.02(2)	0.01(1)
Al_2O_3	0.00(0)	0.01(1)	0.01(1)
Cr_2O_3	0.02(2)	0.00(1)	0.02(2)
FeO	0.35(3)	0.36(3)	0.37(1)
MnO	0.04(2)	0.03(2)	0.02(2)
NiO	0.02(2)	0.01(2)	0.01(2)
MgO	57.79(144)	57.74(56)	57.66(40)
CaO	0.01(1)	0.01(1)	0.01(1)
Na_2O	0.02(2)	0.01(1)	0.00(0)
K_2O	0.00(1)	0.01(1)	0.00(0)
Total	99.16(117)	99.48(79)	99.44(72)
Si	0.97(3)	0.98(1)	0.98(1)
Ti	0.00(0)	0.00(0)	0.00(0)
Al	0.00(0)	0.00(0)	0.00(0)
Cr	0.00(0)	0.00(0)	0.00(0)
Fe	0.01(0)	0.01(0)	0.01(0)
Mn	0.00(0)	0.00(0)	0.00(0)
Ni	0.00(0)	0.00(0)	0.00(0)
Mg	2.05(6)	2.04(2)	2.04(1)
Ca	0.00(0)	0.00(0)	0.00(0)
Na	0.00(0)	0.00(0)	0.00(0)
K	0.00(0)	0.00(0)	0.00(0)
Total	3.03(3)	3.02(1)	3.02(1)
Mg#[c]	99.67(3)	99.65(3)	99.64(1)

[a] Number after the analyzing position is the number of the EMP analyses. All analyses were from JAY01 and JAY04. [b] Number in the parentheses represents one standard deviation; 40.90(158) read as 40.90 ± 1.58. [c] Mg# = 100 × Mg/(Mg + Fe^{2+}).

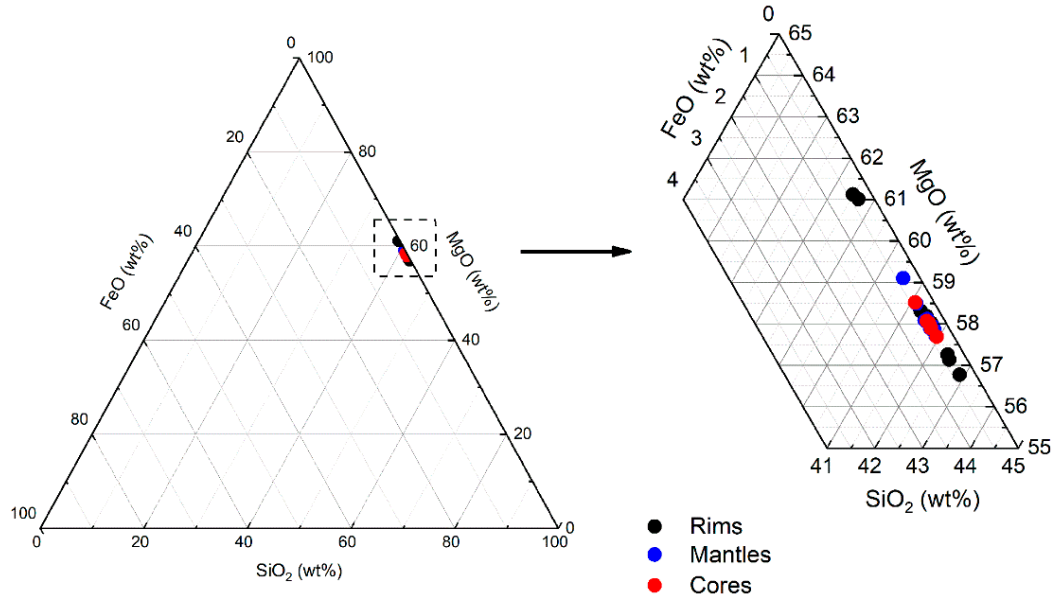

Figure 9. Compositions of the olivines in jianite, plotted in the SiO_2-MgO-FeO composition triangle (wt%). All analyses from different olivine grains (or fragments) from different specimens have been mixed together and grouped according to their relative analyzing positions (rim, mantle, or core). The cores have little Fe-Mg variation, but the rims attain some Fe-Mg variation. Overall, the Fe-Mg variation in the olivines is extremely small.

The LA-ICP-MS analyses, performed on the rims and the cores of some randomly selected olivine grains, are summarized in Table 2. The first feature shown by these analyses is that the olivines have very homogeneous trace element distributions. The second feature is that with the exceptions of B and P, all other analyzed trace elements have abundances much lower than those found in typical low-*T* mantle olivines, in residual mantle olivines after melt extraction to some degrees, or in cumulative olivines crystallizing from mafic magmas [53–57]. Consequently, we believe that the initial trace element characteristics of the olivines have been completely removed by an extremely B-enriched aqueous fluid during the serpentinization process. Thirdly, the B contents of the analyzed olivine are unusually high, ranging from 1697 to 1804 wt ppm, implying that the fluid must have been extremely enriched in boron. This is hardly surprising since significantly elevated B contents were previously observed for some serpentinized materials from the Mayihe formation [28].

The EMP analyses of the antigorite and brucite are summarized in Table 3. It can be seen that the antigorite and brucite have negligible amounts of Fe, implying an excellent chemical equilibrium between them and the forsterite. If the analytical contamination by the brucite grains underneath is removed from the EMP analyses (Figure 10a), one should obtain the general chemical formula $Mg_6Si_4O_{10}(OH)_8$ for the antigorite. In comparison, the deduced chemical formula from the EMP analyses for the brucite is $Mg(OH)_2$ (Figure 10b).

Table 2. Trace element compositions (wt ppm) of olivines in the jianite.

	Rim(10) [a]	Core(9)
Li	1.87(48)[b]	1.97(38)
B	1763(23)	1759(33)
Na	0.92(28)	1.06(73)
Al	38.0(73)	38.1(64)
P	121(13)	120(11)
Ca	23.7(75)	20.7(50)
Sc	1.20(4)	1.20(4)
Ti	7.22(188)	7.59(216)
V	0.57(6)	0.57(6)
Cr	0.92(8)	0.71(8)
Mn	198(5)	199(5)
Co	0.58(3)	0.58(2)
Ni	0.91(6)	0.91(3)
Cu	b.d.l.[c]	b.d.l.
Zn	44.0(9)	44.0(11)
Ga	0.28(2)	0.27(2)
Sr	b.d.l.	b.d.l.
Y	0.068(12)	0.063(12)
Zr	0.87(12)	1.04(35)
Nb	0.094(24)	0.103(32)
Ce	b.d.l.	b.d.l.

[a] Number after the analyzing position is the number of the LA-ICP-MS analyses. The rim and core positions for the LA-ICP-MS analyses were not necessarily identical to those in the EMP analyses. All analyses were from JAY04. [b] Number in the parentheses represents one standard deviation; 1.87(48) read as 1.87 ± 0.48. [c] below detection limit.

Table 3. Major element compositions (wt%) of antigorites and brucites in the jianite.

	Antigorite(13) [a]	Brucite(8)
SiO_2	40.48(317) [b]	1.21(101)
TiO_2	0.02(3)	0.01(1)
Al_2O_3	0.11(14)	0.07(8)
Cr_2O_3	0.01(1)	0.01(2)
FeO	0.48(20)	0.39(8)
MnO	0.02(3)	0.07(3)
NiO	0.01(2)	0.02(2)
MgO	43.30(292)	80.98(464)
CaO	0.02(1)	0.03(2)
Na_2O	0.02(2)	0.03(4)
K_2O	0.02(2)	0.02(2)
Total	84.50(147)	82.83(459) [c]
Si	3.87(24)	0.01(1)
Ti	0.00(0)	0.00(0)
Al	0.01(2)	0.00(0)
Cr	0.00(0)	0.00(0)
Fe	0.04(2)	0.00(0)
Mn	0.00(0)	0.00(0)
Ni	0.00(0)	0.00(0)
Mg	6.19(49)	0.98(2)
Ca	0.00(0)	0.00(0)
Na	0.00(0)	0.00(0)
K	0.00(0)	0.00(0)
Total	10.12(24)	0.99(1)

[a] Number after the phase is the number of the EMP analyses. [b] Number in the parentheses represents one standard deviation; 40.48(317) read as 40.48 ± 3.17. [c] Higher total than the ideal value of ~69.10 was caused mostly by poor beam-focusing.

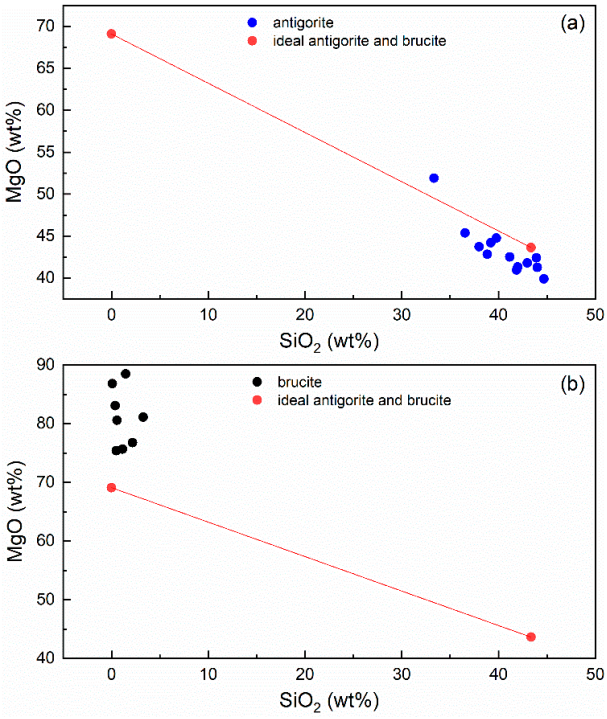

Figure 10. SiO_2 versus MgO of the serpentine (antigorite; **a**) and brucite (**b**) in jianite. Some electron microprobe (EMP) analyses of the antigorite may include small amounts of material from the brucite underneath, leading to a relatively larger composition scattering (Table 3). The EMP analyses of the brucite may have suffered a beam-focusing problem, leading to much higher totals (the total of the anhydrous components should be close to ~69.1%).

Obviously, the extremely low Fe components in these minerals can be essentially ignored, and Equation (1) can be quantitatively approximated by

$$4Mg_2SiO_4 + 6H_2O = Mg_6Si_4O_{10}(OH)_8 + 2Mg(OH)_2 \quad (2)$$

As ~40% olivine of the dunite was consumed (Figure 3), a substantial amount of aqueous fluid then must have presented the serpentinization process. As a result, all initial trace element characteristics of the olivine could have been effectively erased. We thus infer that the distinct trace element abundances and ratios of the olivine observed here could form some of the key signals to a fluid-mediated process with the presence of a large amount of aqueous fluid at relatively low *P-T* conditions (e.g., ~450 ºC and a few kbar), particularly supplementary to those well-established compositional parameters for various processes in the mantle [58,59].

3.4. Water in Olivine

The unpolarized IR spectra taken from the forsterite are shown in Figure 11. As can be seen in the figure, all the crystals (or fragments) contain some prominent water peaks, suggesting that all the olivines have been extensively hydrated. In addition, the IR spectra indicate that water in the olivine is incorporated as hydrogen defects rather than molecular water. Further, water homogeneously distributes in the olivine crystals, as reflected by the nearly identical intensities of the water peaks from the olivine rims and from the olivine cores (red curves versus black curves).

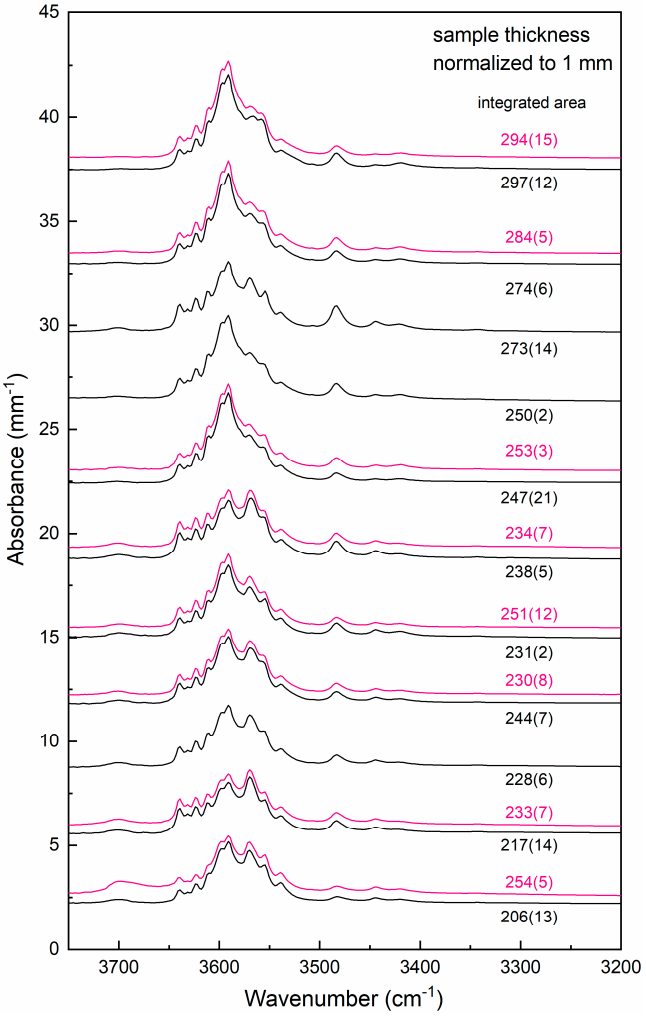

Figure 11. Unpolarized infrared spectra of the forsterite in jianite. Each pair of IR spectra is from one forsterite crystal (or fragment), with the spectrum in black representing the central position and the spectrum in pink representing the rim position. Numbers next to the IR spectrum is the integrated absorbance for the region 3750–3200 cm^{-1}, with the numbers in the parentheses representing one standard deviation (294(15) read as 294 ± 15).

Using the olivine-specific calibration of Bell et al. [60], the water content in the olivine has been estimated as 1450(300) wt ppm. Although it is not clear whether or not all the 11 analyzed olivine crystals or fragments were from different olivine grains with different orientations, we are sure that they were from at least three arbitrarily selected crystals. The water content then has been constrained to good accuracy (better than 25%) [61].

All the IR spectra have been carefully deconvoluted, with one example shown in Figure 12. There are 13 strong water peaks at ~3639, 3631, 3623, 3611, 3599, 3590, 3581, 3567, 3556, 3538, 3523, 3483, and 3420 cm^{-1}, and eight less intense water peaks at ~3645, 3507, 3475, 3443, 3405, 3384, 3348, and 3328 cm^{-1}. In general, the water peaks in olivine can be roughly divided into two groups: Group I in the range of ~3650–3450 cm^{-1} and Group II in the range of 3450–3200 cm^{-1}, with the former indicating hydrogens associating with Si vacancies and the latter suggesting hydrogens attributable to Mg vacancies [62–64]. Clearly, the Group I water peaks of our olivine are very strong while the Group II water peaks are very weak (Figure 12) so that our olivine must contain significant amounts of Si vacancies, in good agreement with the composition data obtained from our EMP analyses (Table 1). Hence, the fluid that hydrated the olivine must have had a low silica activity.

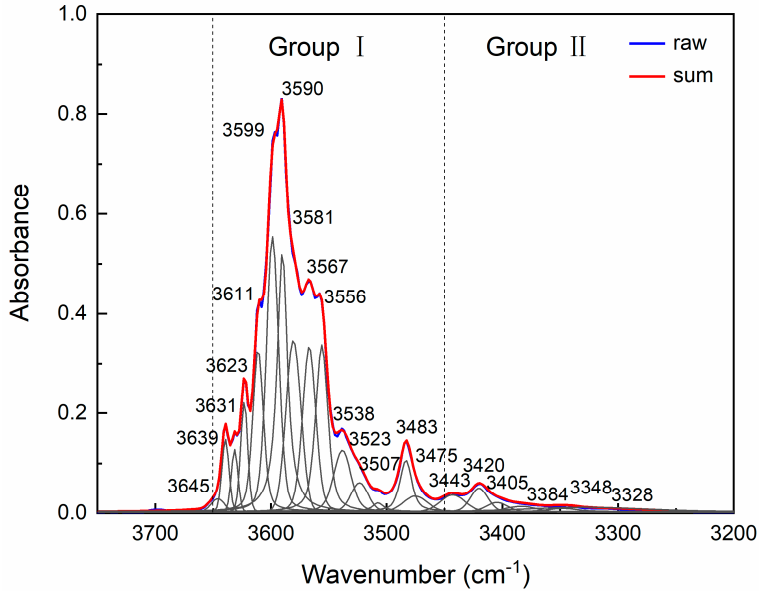

Figure 12. Gaussian–Lorentzian deconvolution of the OH infrared peaks of the forsterite in jianite (the 3750–3200 cm^{-1} region). We used the PeakFit V4.12 software (SPSS Inc.) to process the IR data. The detected 21 Gaussian–Lorentzian peaks (the black curves) can be roughly divided into two groups, Group I in the range of ~3650–3450 cm^{-1} and Group II in the range of ~3450–3200 cm^{-1}. The sum (the red curve) of the 21 component peaks agrees well with the raw data (the blue curve) for the most data range.

Notably, the IR spectra of our olivine contain a distinct water peak at ~3538 cm^{-1}, which has been assigned to some boron-related defects ($B^{3+} + H^{+} = Si^{4+}$) by Matsyuk and Langer [65]. Indeed, our olivine is boron-rich (Table 2).

4. Discussion: Jianite and Its Petrogenesis

The protolith of the serpentinized dunite reported here is unusual. As depicted above, the rock contains no other primary minerals such as orthopyroxene and clinopyroxene but olivine. Further, the olivine is virtually forsterite with little iron. According to Huang et al. [41,66] and Evans [40], the serpentinization process is not very efficient in removing Fe from the system. This is presumably partially because the end part of the hierarchic fluid-transport system is readily clogged due to the continuous volume expansion as the process advances [52], and partially because the serpentinization process takes place at very low T (here at ~425(25) °C). The same should be true for other major elements like Al and Ca. If the protolith had contained some other primary minerals like orthopyroxene and clinopyroxene, the Al and Ca hosted by these minerals should have been retained in the rock and easily detected by our analyses. Consequently, we tend to believe that the protolith was entirely made of forsterite. On this ground, we would like to coin the word "jianite" (集安岩) to emphasize this lithology, with Jian after Ji'an (集安), the name of the county where we collected our specimens.

The jianite found in Ji'an County is distinct from nearly all conventional dunites. To the best of our knowledge, the closest example to the jianite, in terms of phase assemblage and phase composition, is the dunite xenolith QX-18 from Qixia, North China Craton, which consists entirely of mosaic textured olivine with an Mg# of 98 [7]. However, the size of that dunite xenolith is mostly ~2–5 cm only, and the olivine grains might be coarser (presumably larger than a few mm). In comparison, the jianite reported here occupies a vast area of at least up to ~50 m^2 and contains relatively fine-grained forsterite (~2 mm in size).

The petrogenesis of the monomineralic jianite is unclear and so is that of the dunite xenolith QX-18. The dunite xenolith QX-18 was brought up by the 9–18 Ma Qixia nephelinites, along with

other relatively fertile peridotitic xenoliths of young formation ages (Mesozoic or younger) [7]. Since there is not any good means to date the forsterites (Personal communication with Prof. Weidong Sun), it remains at least a possibility that this xenolith might represent the ancient and refractory lithospheric mantle of the North China Craton. In analog to this speculation, we propose that the jianite reported here might stand for the ancient and refractory lithospheric mantle of the North China Craton as well, which was somehow transported into the Liao-Ji Proterozoic rift zone. Along with other rocks in the Mayihe formation of the Ji'an group, the jianite might have experienced the regional amphibolite–granulite facies metamorphic event at ~1881–1870 Ma [24,67], being serpentinized by a B-rich, Si-poor aqueous fluid potentially originating from the dehydration process of a subducted slab [28]. The relatively small grain size of its forsterite (up to ~2 mm) remains to be explained though.

Another potential process that could have led to the formation of the jianite is that the forsterite might have quickly crystallized at relatively low temperatures from a special hydrous magma with its anhydrous components close to the forsterite composition [38]. If this scenario were correct, the quick crystallizing process could be used to explain the relatively small grain size of the forsterite. However, how and where such a hydrous magma could be geologically generated are presently beyond the reach of our cognition.

Other processes leading to the formation of nearly pure forsterite include serpentinization/deserpentinization of dunites and silicification of dolomite [18–23]. However, there has not been any mechanism to concentrate thus-formed forsterite grains to form a massive monomineralic rock like the jianite reported in this study. Minerals such as spinel, magnetite, dolomite, and calcite usually appear along with the forsterite.

With a rather uncertain petrogenesis, the jianite, i.e., massive dunite solely made of pure forsterite, may have some implications to the geochemical, geophysical, and geodynamic processes of the Earth. For example, it may affect the geodynamic process of subducted slabs, as implied by the stable/metastable phase relations of forsterite and the corresponding variations of the physical properties like density and sound velocity of forsterite and its polymorphs at typical subduction zone *P-T* conditions [68–70]. It is certain that much remains to be probed.

Supplementary Materials: The following are available online at http://www.mdpi.com/2075-163X/10/3/220/s1, Table S1: Raman data for the Fe- and Al-poor antigorites.

Author Contributions: Y.W. (collecting, processing, and analyzing the samples, interpreting the results, and writing the first draft of the paper); M.H. (designing and supervising the project, interpreting the results, and writing the second version of the paper); X.L. (supervising the project, interpreting the results, and finalizing the paper); W.Y. (collecting and interpreting the IR data and checking the first draft of the paper); M.Y. (guiding the field trip and collecting the samples). All authors have read and agreed to the published version of the manuscript.

Funding: This study is financially supported by the Program of the National Mineral Rock and Fossil Specimens Resource Center from MOST, China and by the DREAM Project of MOST, China (Grant No. 2016YFC0600408).

Acknowledgments: We thank two anonymous reviewers for their detailed and constructive suggestions. We thank Y. Jiang, general manager of the Yanbian Fuli Olivine Mining Co. (Ltd.), for the help during the field trip. We thank Y. Lu from China University of Geosciences (Beijing) for the guidance of the field trip. We thank X. Li from Peking University for the technical support to the EMP analyses, H. Ding from Peking University for the technical support to the Raman analyses, and F. Ma from Peking University for the technical support to the LA-ICP-MS analyses.

Conflicts of Interest: The authors declare no conflict of interest.

References

1. Walter, M.J. Melting residues of fertile peridotite and the origin of cratonic lithosphere. *Spec. Publ. Geochem. Soc.* **1999**, *6*, 225–239.
2. Bernstein, S.; Kelemen, P.B.; Hanghøj, K. Consistent olivine Mg# in cratonic mantle reflects Archean mantle melting to the exhaustion of orthopyroxene. *Geology* **2007**, *35*, 459–462.
3. Boyd, F.R.; Nixon, P.H. Ultramafic nodules from the Kimberley pipes, South Africa. *Geochim. Cosmochim. Acta* **1978**, *42*, 1367–1382. [CrossRef]

4. Griffin, W.L.; O'Reilly, S.Y.; Ryan, C.G. The composition and origin of sub-continental lithospheric mantle. *Spec. Publ. Geochem. Soc.* **1999**, *6*, 13–45.
5. Fan, W.M.; Zhang, H.F.; Baker, J.; Jarvis, K.E.; Mason, P.R.D.; Menzies, M.A. On and off the north China craton: Where is the Archaean keel? *J. Petrol.* **2000**, *41*, 933–950. [CrossRef]
6. Zheng, J.; O'Reilly, S.Y.; Griffin, W.L.; Lu, F.; Zhang, M.; Pearson, N.J. Relic refractory mantle beneath the eastern North China block: Significance for lithosphere evolution. *Lithos* **2001**, *57*, 43–66. [CrossRef]
7. Rudnick, R.L.; Gao, S.; Ling, W.; Liu, Y.; McDonough, W.F. Petrology and geochemistry of spinel peridotite xenoliths from Hannuoba and Qixia, North China craton. *Lithos* **2004**, *77*, 609–637. [CrossRef]
8. Jaques, A.L.; Green, D.H. Anhydrous melting of peridotite at 0–15 Kb pressure and the genesis of tholeiitic basalts. *Contrib. Mineral. Petrol.* **1980**, *73*, 287–310. [CrossRef]
9. Falloon, T.J.; Green, D.H.; Hatton, C.J.; Harris, K.L. Anhydrous partial melting of a fertile and depleted peridotite from 2 to 30 kb and application to basalt petrogenesis. *J. Petrol.* **1988**, *29*, 1257–1282. [CrossRef]
10. Barnes, S.J.; Roeder, P.L. The range of spinel compositions in terrestrial mafic and ultramafic rocks. *J. Petrol.* **2001**, *42*, 2279–2302. [CrossRef]
11. Liu, X.; O'Neill, H.S.C. The effect of Cr_2O_3 on the partial melting of spinel lherzolite in the system CaO-MgO-Al_2O_3-SiO_2-Cr_2O_3 at 1.1 GPa. *J. Petrol.* **2004**, *45*, 2261–2286. [CrossRef]
12. Green, D.H.; Ringwood, A.E. The genesis of basaltic magmas. *Contrib. Mineral. Petrol.* **1967**, *15*, 103–190. [CrossRef]
13. Roeder, P.L.; Emslie, R.F. Olivine-liquid equilibrium. *Contrib. Mineral. Petrol.* **1970**, *29*, 275–289. [CrossRef]
14. Plechov, P.Y.; Shcherbakov, V.D.; Nekrylov, N.A. Extremely magnesian olivine in igneous rocks. *Russ. Geol. Geophys.* **2018**, *59*, 1702–1717. [CrossRef]
15. Sui, J.; Fan, Q.; Liu, J. Discovery and significance of high-purity forsterite ($Fo_{\sim 98.5}$) and its dissolution structure in Longgang volcano, Jilin Province. In Proceedings of the 11th Annual Conference of the Chinese Society for Mineralogy, Petrology and Geochemistry, Beijing, China, 27–30 August 2007; p. 37.
16. Blondes, M.S.; Brandon, M.T.; Reiners, P.W.; Page, F.Z.; Kita, N.T. Generation of forsteritic olivine ($Fo_{99.8}$) by subsolidus oxidation in basaltic flows. *J. Petrol.* **2012**, *53*, 971–984. [CrossRef]
17. Bai, W.; Fan, Q.; Zhan, Z.; Yan, B.; Yang, J. Crystal structure of forsterite from podiform chromitite in Luobusa ophiolite of Tibet and its implications. *Acta Petrol. Mineral.* **2001**, *20*, 1–10.
18. Owens, B.E. High-temperature contact metamorphism of calc-silicate xenoliths in the Kiglapait Intrusion, Labrador. *Am. Mineral.* **2000**, *85*, 1595–1605. [CrossRef]
19. Wenzel, T.; Baumgartner, L.P.; Konnikov, E.G.; Brugmann, G.E.; Kislov, E.V. Partial melting and assimilation of dolomitic xenoliths by mafic magma: The Ioko-Dovyren intrusion (North Baikal region, Russia). *J. Petrol.* **2002**, *43*, 2049–2074. [CrossRef]
20. Ferry, J.M.; Ushikubo, T.; Valley, J.W. Formation of forsterite by silicification of dolomite during contact metamorphism. *J. Petrol.* **2011**, *52*, 1619–1640. [CrossRef]
21. Arai, S.; Ishimaru, S.; Mizukami, T. Methane and propane micro-inclusions in olivine in titanoclinohumite-bearing dunites from the Sanbagawa high-P metamorphic belt, Japan: Hydrocarbon activity in a subduction zone and Ti mobility. *Earth Planet. Sci. Lett.* **2012**, *353–354*, 1–11. [CrossRef]
22. Chen, Y.; Huang, F.; Shi, G.-H.; Wu, F.-Y.; Chen, X.; Jin, Q.-Z.; Su, B.; Guo, S.; Sein, K.; Nyunt, T.T. Magnesium isotope composition of subduction zone fluids as constrained by jadeitites from Myanmar. *J. Geophys. Res.* **2018**, *123*, 7566–7585. [CrossRef]
23. Majumdar, A.S.; Hovelmann, J.; Vollmer, C.; Berndt, J.; Mondal, S.K.; Putnis, A. Formation of Mg-rich olivine pseudomorphs in serpentinized dunite from the Mesoarchean Nuasahi Massif, eastern India: Insights into the evolution of fluid composition at mineral-fluid interface. *J. Petrol.* **2016**, *57*, 3–26. [CrossRef]
24. Qin, Y.; Chen, D.; Liang, Y.; Zou, C.; Zhang, Q.; Bai, L. Geochronology of Ji'an group in Tonghua area, southern Jilin province. *J. Earth Sci.* **2014**, *39*, 1487–1499.
25. Zhou, X.; Di, X.; Lu, X.; Kong, F. Discovery and significance of the ophiolite in Ji'an rock group, southern of Jilin Province. *Jilin Geol.* **2018**, *37*, 1–6.

26. Zhang, W.; Liu, F.; Cai, J.; Liu, C.; Liu, J.; Liu, P.; Liu, L.; Wang, F.; Yang, H. Geochemistry, zircon U-Pb dating and tectonic implications of the Palaeoproterozoic Ji'an and Laoling groups, northeastern Jiao-Liao-Ji Belt, North China Craton. *Precambrian Res.* **2018**, *314*, 264–287. [CrossRef]
27. Meng, E.; Wang, C.-Y.; Li, Z.; Li, Y.-G.; Yang, H.; Cai, J.; Ji, L.; Jin, M.-Q. Palaeoproterozoic metasedimentary rocks of the Ji'an group and their significance for the tectonic evolution of the northern segment of the Jiao–Liao–Ji Belt, North China Craton. *Geol. Mag.* **2017**, *155*, 149–173. [CrossRef]
28. Lu, X. Paleoproterozoic Tectonic Magmatic Event in Tonghua Area. Ph.D. Dissertation, Jilin University, Changchun, China, 15 June 2004.
29. Liu, L.; Liu, X.; Bao, X.; He, Q.; Yan, W.; Ma, Y.; He, M.; Tao, R.; Zou, R. Si-disordering in $MgAl_2O_4$-spinel under high *P-T* conditions, with implications for Si-Mg disorder in $MgAl_2O_4$-ringwoodite. *Minerals* **2018**, *8*, 210. [CrossRef]
30. Li, X.; Zhang, L.; Wei, C.; Slabunov, A.I.; Bader, T. Quartz and orthopyroxene exsolution lamellae in clinopyroxene and the metamorphic *P-T* path of Belomorian eclogites. *J. Metamorph. Geol.* **2017**, *36*, 1–22. [CrossRef]
31. Liu, L.; Ma, Y.; Yan, W.; Liu, X. Trace element partitioning between $MgAl_2O_4$-spinel and carbonatitic silicate melt from 3 to 6 GPa, with emphasis on the role of cation order-disorder. *Solid Earth Sci.* **2019**, *4*, 43–65. [CrossRef]
32. Li, X.-W.; Mo, X.-X.; Yu, X.-H.; Ding, Y.; Huang, X.-F.; Wei, P.; He, W.-Y. Petrology and geochemistry of the early mesozoic pyroxene andesites in the Maixiu Area, west Qinling, China: Products of subduction or syn-collision? *Lithos* **2013**, *172–173*, 158–174. [CrossRef]
33. Jochum, K.P.; Weis, U.; Stoll, B.; Kuzmin, D.; Yang, Q.; Raczek, I.; Jacob, D.E.; Stracke, A.; Birbaum, K.; Frick, D.A.; et al. Determination of reference values for NIST SRM 610-617 glasses following ISO guidelines. *Geostand. Geoanal. Res.* **2011**, *35*, 397–429. [CrossRef]
34. Jackson, S.E. The Application of Nd: YAG Lasers in LA-ICP-MS. In *Principles and Applications of Laser Ablation-Mass Spectrometry in the Earth Sciences*, 2nd ed.; Sylvester, P., Ed.; Mineralogical Association of Canada: Quebec City, QC, Canada, 2001; Volume 29, pp. 29–45.
35. Liu, X.; Ma, Y.; He, Q.; He, M. Some IR features of SiO_4, and OH in coesite, and its amorphization and dehydration at ambient pressure. *J. Asian Earth Sci.* **2017**, *148*, 315–323. [CrossRef]
36. He, M.; Yan, W.; Chang, Y.; Liu, K.; Liu, X. Fundamental infrared absorption features of α-quartz: An unpolarized single-crystal absorption infrared spectroscopic study. *Vib. Spectrosc.* **2019**, *101*, 52–63. [CrossRef]
37. Liu, X.; O'Neill, H.S.C.; Berry, A.J. The effects of small amounts of H_2O, CO_2 and Na_2O on the partial melting of spinel lherzolite in the system CaO–MgO–Al_2O_3–SiO_2 ± H_2O ± CO_2 ± Na_2O at 1.1 GPa. *J. Petrol.* **2006**, *47*, 409–434. [CrossRef]
38. Bowen, N.L.; Tuttle, O.F. The system MgO-SiO_2-H_2O. *Geol. Soc. Am. Bull.* **1949**, *60*, 439–460. [CrossRef]
39. Evans, B.W. The serpentinite multisystem revisited: Chrysotile is metastable. *Inter. Geol. Rev.* **2004**, *46*, 479–506. [CrossRef]
40. Evans, B.W. Lizardite versus antigorite serpentinite: Magnetite, hydrogen, and life (?). *Geology* **2010**, *38*, 879–882. [CrossRef]
41. Huang, R.; Lin, C.-T.; Sun, W.; Ding, X.; Zhan, W. The production of iron oxide during peridotite serpentinization: Influence of pyroxene. *Geosci. Front.* **2017**, *8*, 1311–1321. [CrossRef]
42. Mohanan, K.; Sharma, S.K.; Bishop, F.C. A Raman spectral study of forsterite-monticellite solid solutions. *Am. Mineral.* **1993**, *78*, 42–48.
43. Ishibashi, H.; Arakawa, M.; Yamamoto, J.; Kagi, H. Precise determination of Mg/Fe ratios applicable to terrestrial olivine samples using Raman spectroscopy. *J. Raman Spectrosc.* **2012**, *43*, 331–337. [CrossRef]
44. Auzende, A.L.; Daniel, L.; Reynard, B.; Lemaire, C.; Guyot, F. High-pressure behaviour of serpentine minerals: A Raman spectroscopic study. *Phys. Chem. Mineral.* **2004**, *31*, 267–277. [CrossRef]
45. Groppo, C.; Rinaudo, C.; Cairo, S.; Gastaldi, D.; Compagnoni, R. Micro-Raman spectroscopy for a quick and reliable identification of serpentine minerals from ultramafics. *Eur. J. Mineral.* **2006**, *18*, 319–329. [CrossRef]
46. Reynard, B.; Wunder, B. High-pressure behavior of synthetic antigorite in the MgO-SiO_2-H_2O system from Raman spectroscopy. *Am. Mineral.* **2006**, *91*, 459–462. [CrossRef]

47. Rinaudo, C.; Gastaldi, D.; Belluso, E. Characterization of chrysotile, antigorite and lizardite by FT-Raman spectroscopy. *Can. Mineral.* **2003**, *41*, 883–890. [CrossRef]
48. Prencipe, M.; Noel, Y.; Bruno, M.; Dovesi, R. The vibrational spectrum of lizardite-1 *T* [$Mg_3Si_2O_5(OH)_4$] at the Γ point: A contribution from an ab initio periodic B3LPY calculation. *Am. Mineral.* **2009**, *94*, 986–994. [CrossRef]
49. Schwartz, S.; Guillot, S.; Reynard, B.; Lafay, R.; Debret, B.; Nicollet, C.; Lanari, P.; Line Auzende, A. Pressure-temperature estimates of the lizardite/antigorite transition in high pressure serpentinites. *Lithos* **2013**, *178*, 197–210. [CrossRef]
50. Dawson, P.; Hadfield, C.D.; Wilkinson, G.R. The polarized infrared and Raman spectra of $Mg(OH)_2$ and $Ca(OH)_2$. *J. Phys. Chem. Solids.* **1973**, *34*, 1217–1225. [CrossRef]
51. Duffy, T.S.; Meade, C.; Fei, Y.; Mao, H.-K.; Hemley, R.J. High-pressure phase transition in brucite, $Mg(OH)_2$. *Am. Mineral.* **1995**, *80*, 222–230. [CrossRef]
52. Mével, C. Serpentinization of abyssal peridotites at mid-ocean ridges. *C. R. Geosci.* **2017**, *335*, 825–852. [CrossRef]
53. Witt-Eickschen, G.; O'Neill, H.S.C. The effect of temperature on the equilibrium distribution of trace elements between clinopyroxene, orthopyroxene, olivine and spinel in upper mantle peridotite. *Chem. Geol.* **2005**, *221*, 65–101. [CrossRef]
54. De Hoog, J.C.M.; Gall, L.; Cornell, D.H. Trace-element geochemistry of mantle olivine and application to mantle petrogenesis and geothermobarometry. *Chem. Geol.* **2010**, *270*, 196–215. [CrossRef]
55. Tollan, P.M.E.; O'Neill, H.S.C.; Hermann, J.; Benedictus, A.; Arculus, R.J. Frozen melt–rock reaction in a peridotite xenolith from sub-arc mantle recorded by diffusion of trace elements and water in olivine. *Earth Planet. Sci. Lett.* **2015**, *422*, 169–181. [CrossRef]
56. Straub, S.M.; LaGatta, A.B.; Lillian Martin-Del Pozzo, A.; Langmuir, C.H. Evidence from high-Ni olivines for a hybirdized peridotite/pyroxenite source for orogenic andesites from the central Mexican Volcanic Belt. *Geochem. Geophys. Geosys.* **2008**, *9*, Q03007. [CrossRef]
57. Su, B.; Chen, Y.; Mao, Q.; Zhang, D.; Jia, L.-H.; Guo, S. Minor elements in olivine inspect the petrogenesis of orogenic peridotites. *Lithos* **2019**, *344–345*, 207–216. [CrossRef]
58. Foley, S.F.; Prelevic, D.; Rehfeldt, T.; Jacob, D.E. Minor and trace elements in olivines as probes into early igneous and mantle melting processes. *Earth Planet. Sci. Lett.* **2013**, *363*, 181–191. [CrossRef]
59. Shea, J.J.; Foley, S.F. Evidence for carbonatite-influenced source assemblage for intraplate basalts from the Buckland Volcanic Province, Queensland, Australia. *Minerals* **2019**, *9*, 546. [CrossRef]
60. Bell, D.R.; Rossman, G.R.; Maldener, J.; Endisch, D.; Rauch, F. Hydroxide in olivine: A quantitative determination of the absolute amount and calibration of the IR spectrum. *J. Geophys. Res.* **2003**, *108*, 2105. [CrossRef]
61. Qiu, Y.; Jiang, H.; Kovács, I.; Xia, Q.-K.; Yang, X. Quantitative analysis of H-species in anisotropic minerals by unpolarized infrared spectroscopy: An experimental evaluation. *Am. Mineral.* **2018**, *103*, 1761–1769. [CrossRef]
62. Bai, Q.; Kohlstedt, D.L. Effects of chemical environment on the solubility and incorporation mechanism for hydrogen in olivine. *Phys. Chem. Mineral.* **1993**, *19*, 460–471. [CrossRef]
63. Matveev, S.; O'Neill, H.S.C.; Ballhaus, C.; Taylor, W.R.; Green, D.H. Effect of silica activity on OH-IR spectra of olivine: Implications for low-*a* SiO_2 mantle metasomatism. *J. Petrol.* **2001**, *42*, 721–729. [CrossRef]
64. Lemaire, C.; Kohn, S.C.; Brooker, R.A. The effect of silica activity on the incorporation mechanisms of water in synthetic forsterite: A polarised infrared spectroscopic study. *Contrib. Mineral. Petrol.* **2004**, *147*, 48–57.
65. Matsyuk, S.S.; Langer, K. Hydroxyl in olivines from mantle xenoliths in kimberlites of the Siberian platform. *Contrib. Mineral. Petrol.* **2004**, *147*, 413–437. [CrossRef]
66. Huang, R.; Sun, W.; Ding, X.; Wang, Y.; Zhan, W. Experimental investigation of iron mobility during serpentinization. *Acta Petrol. Sin.* **2015**, *31*, 883–890.
67. Cai, J.; Liu, F.; Liu, P.; Wang, F. Metamorphic P-T evolution and tectonic implications of pelitic granulites in the Ji'an area, northeastern Jiao-Liao-Ji Belt, North China Craton. *J. Asian Earth Sci.* **2020**, *191*, 104197. [CrossRef]
68. Finkelstein, G.J.; Dera, P.K.; Jahn, S.; Oganov, A.R.; Holl, C.M.; Meng, Y.; Duffy, T.S. Phase transitions and equation of state of forsterite to 90 GPa from single-crystal X-ray diffraction and molecular modeling. *Am. Mineral.* **2014**, *99*, 35–43. [CrossRef]

69. Zhang, Y.; Zhang, Y.; Liu, Y.; Liu, X. A metastable Fo-III wedge in cold slabs subducted to the lower part of the mantle transition zone: A hypothesis based on first-principles simulations. *Minerals* **2019**, *9*, 186. [CrossRef]
70. Mao, Z.; Jacobsen, S.D.; Jiang, F.; Smyth, J.R.; Holl, C.M.; Frost, D.J.; Duffy, T.S. Velocity crossover between hydrous and anhydrous forsterite at high pressures. *Earth Planet. Sci. Lett.* **2010**, *293*, 250–258. [CrossRef]